



# Interfacial debonding detection for CFST structures using an ultrasonic phased array: Application to the Shenzhen SEG building

Hai Liu <sup>a,c</sup>, Zhijie Chen <sup>a,\*</sup>, Yijie Liu <sup>a,\*</sup>, Yangyang Chen <sup>b</sup>, Yanliang Du <sup>a</sup>, Fulin Zhou <sup>b</sup>

<sup>a</sup> School of Civil Engineering, Guangzhou University, Guangzhou 510006, China

<sup>b</sup> Earthquake Engineering Research & Test Center, Guangzhou University, Guangzhou 510006, China

<sup>c</sup> Guangdong Engineering Research Center For Underground Infrastructural Protection in Coastal Clay Area, Guangzhou University, Guangzhou 510006, China

## ARTICLE INFO

Communicated by Filippo Ubertini

### Keywords:

Concrete filled steel tube (CFST)  
Interfacial debonding  
Imaging-based detection  
Ultrasonic phased array  
total focusing method (TFM)  
Reflection coefficient

## ABSTRACT

Concrete filled steel tube (CFST) structures have been widely applied to the construction of high-rise buildings and bridges. However, interfacial debonding defects generally occur due to deficient construction quality, concrete shrinkage, and other reasons. In this paper, an imaging-based approach using a designed ultrasonic phased array is proposed for the semi-quantitative characterization of interfacial debonding defects in CFST columns. A total focusing method (TFM) is employed for high-resolution image reconstruction from the full matrix capture (FMC) dataset acquired by the phased array. Based on the reflection coefficient of the steel-concrete interface in the imaging result, a criterion is proposed to evaluate the degree of debonding damage. The proposed approach is used to evaluate the debonding defects in the 16 CFST columns of the Shenzhen SEG Building, which experienced abnormal shaking on May 18–20, 2021. The accuracy of the proposed method is fully validated with 15 boreholes on the CFST columns. Then, ultrasonic phase array measurements were conducted along 34 circumferential rings on nine of the CFST columns. The results show that the comprehensive debonding rate is as high as 46.6%. It is concluded that the proposed ultrasonic phased array method can accurately detect and locate the debonding defects in CFST structures, and this method has a broad application prospect for non-destructive inspection in civil engineering.

## 1. Introduction

Concrete-filled steel tube (CFST) structures have been widely applied to construction of large-scale infrastructures such as high-rise buildings [1] and long-span bridges [2–3]. Compared with conventional steel and reinforced concrete structures, CFST structures can make full use of the material strength of concrete and steel to improve the bearing capacity and seismic resistance [4]. However, due to the influence of deficient construction quality, concrete shrinkage and dynamic loads, interfacial debonding commonly occurs between a concrete core and a steel tube, as shown in Fig. 1 [5]. The influence of debonding in CFST columns has been investigated experimentally and numerically. It was found that this type of defect would seriously degrade the bearing capacity, affect the structural safety and shorten the service life [6–8]. Therefore, the detection of interfacial debonding defects in CFST structures is imperative for evaluating the safety of aging CFST structures.

\* Corresponding authors.

E-mail addresses: [zjchen@e.gzhu.edu.cn](mailto:zjchen@e.gzhu.edu.cn) (Z. Chen), [liuyijie1987@outlook.com](mailto:liuyijie1987@outlook.com) (Y. Liu).

The SEG Building (as shown in Fig. 2(a)) is a landmark building in Shenzhen with a height of 292 m. It contains four basement floors and 72 above-ground floors. The roof of this building is equipped with a 54-m-high mast. The building is a composite structure of 16 CFST columns and a reinforced concrete core tube, as shown in Fig. 2(b). The CFST columns have a diameter of 1.3 m or 1.6 m, and the thickness of the steel tube is about 2 cm. From May 18 to 20, 2021, this 20-year-old building experienced successive abnormal shaking for three days [9]. Through several inspections, monitoring, and analysis, it was stated that the coupling of the wind-induced vortex-induced resonance of the mast and the deterioration of the dynamic characteristics of the building caused the perceived vibration [10–11]. Through numerical simulations, Liao *et al.* [12] found that the debonding defects of the CFST columns severely affect the mechanical characteristics of the structure. Therefore, it was decided to detect and locate the debonding defects in the 16 CFST columns of the building.

Various methods have been proposed for the detection of the interfacial debonding of CFSTs [13]. These methods fall into two categories, i.e., destructive and non-destructive methods. A destructive method usually involves the inspection of defects through a drilled hole in a steel tube. Nevertheless, its applications have to be strictly limited to a small number of measuring points in a construction site, since it inevitably results in certain damage to a structure. In comparison, non-destructive testing (NDT) methods [14], e.g., tapping-listening [15–16], wave analysis [17], mechanical impedance method [18–19], and ultrasonic transmitting measurement [20–22], are preferred in practice. The traditional tapping-listening method can be used to qualitatively judge whether or not defects exist by tapping a CSFT using a hammer and listening to the difference of the echoes. Although convenient and efficient in operation, this method cannot accurately locate defects, nor can it be used to estimate the debonding ratio. In addition, it relies on the subjective experience of the practitioner and suffers from the physiological fatigue. Thus, the results are highly unreliable. Wave analysis and mechanical impedance methods are used to analyze vibration signals or impedance changes in CFSTs by attaching piezoelectric transducers (PZT) to the surface of a CFST or embedding them inside the CFST. Xu *et al.* [23] proposed a debonding index governed by the derivatives of reconstructed interfacial forces to identify multi-debonding in CFST beams using noncontact laser vibrometers. Yan *et al.* [24] proposed a PZT transducer-based NDT method using acoustic emission (AE) and electromechanical impedance (EMI) simultaneously. The AE method is capable of capturing the dynamic process of bond slip, and the EMI method aids in the qualitative detection of interfacial debonding. The ultrasonic transmitting measurement involves arranging two transducers on a CFST. The head wave speed and amplitude are analyzed for defect detection in the CFSTs. Song *et al.* [25] detected the interfacial debonding defects based on the attenuation characteristics of guided waves using an air-coupled ultrasonic technique, but the microphone-based NDT test is easily interfered by external sound sources. Dong *et al.* [5] proposed a densified travel-time tomography approach to elaborately delineate the geometry dimensions of debonding defects. However, for this approach, various transducers have to be embedded in CFSTs or attached to the surface of steel components, which is inefficient and not entertained in practical engineering applications.

Compared with the above-mentioned NDT methods, ultrasonic phased array technology enables fast detection speed and provides a high imaging resolution. The principle of the ultrasonic imaging method is illustrated in Fig. 3(a). An ultrasonic array probe consists of  $N$  linear transducers. The transducers take turns to radiate ultrasonic pulse signals, and all of the transducers act as receivers to collect the reflected signals. As a result, an  $N \times N$  full-matrix capture (FMC) dataset [26], as shown in Fig. 3(b), can be acquired by the ultrasonic array. Based on the FMC dataset, imaging algorithms such as synthetic aperture focusing technology (SAFT) [27], total focusing method (TFM) [28–29], or reverse time migration (RTM) [30–31] are used for image reconstruction. Among these algorithms, RTM can produce the highest imaging resolution, but it requires large computation costs. SAFT suffers from a poor imaging resolution, which cannot meet the accuracy requirement for debonding localization. Therefore, in this research, a TFM algorithm is adopted for image reconstruction.

In this paper, an imaging-based method is proposed for interfacial debonding defect detection using an ultrasonic phased array. Criteria for evaluating the damage degree at a single measuring point and along a cross-sectional survey line are proposed based on the



**Fig. 1.** Interfacial debonding of a CFST column.

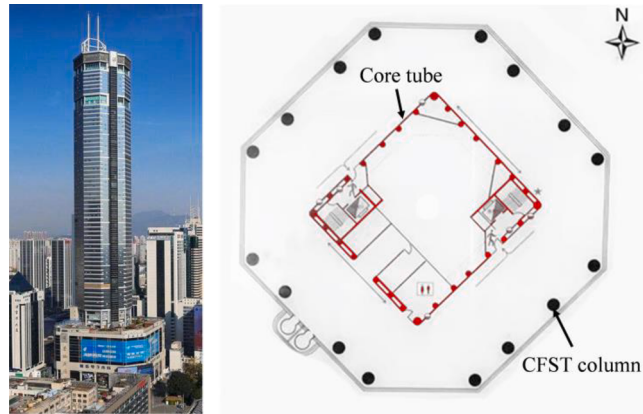


**Fig. 2.** Shenzhen SEG Building. (a) A photo and (b) the architectural plan of the structure.

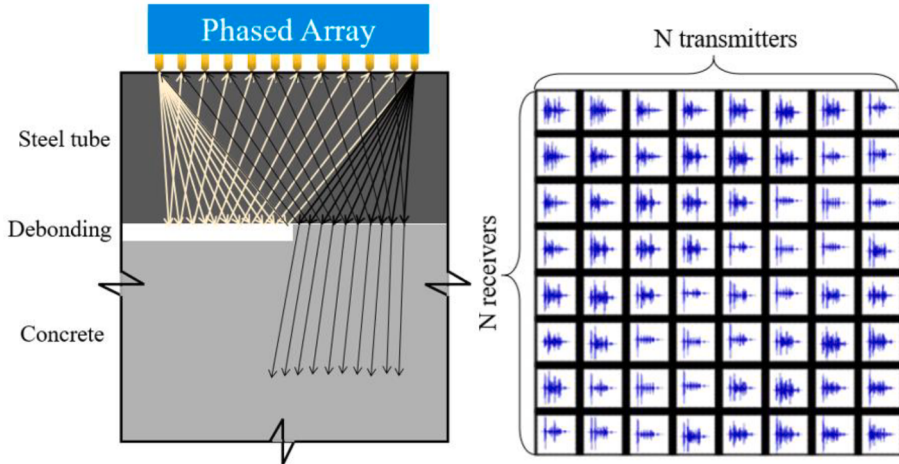


**Fig. 3.** Schematic illustration of (a) the imaging-based detection method using an ultrasonic phased array and (b) full-matrix capture (FMC) dataset.

interface reflection signal in the reconstructed image. The rest of this paper is organized as follows. [Section 2](#) introduces the designed ultrasonic phased array system. In [Section 3](#), the TFM algorithm is introduced and a criterion is proposed to evaluate the interfacial debonding damage in CFSTs. [Section 4](#) presents the results of a verification experiment and field measurements in the Shenzhen SEG Building. [Section 5](#) is the discussion, and this section is followed by the conclusions in [Section 6](#).



**Fig. 4.** The developed ultrasonic phase array system.

## 2. Designed ultrasonic phased array system

Ultrasonic phased array technology applies piezoelectric components to excite ultrasonic waves, and this technology has achieved great success in the medical imaging field [32]. The reflected ultrasonic signal from an interface with acoustic impedance contrast is converted into an electrical signal and recorded by the piezoelectric elements. In this research, an ultrasonic phased array system is developed for detection of interfacial debonding in CFSTs, as shown in Fig. 4. As the key component of the system, an ultrasonic phased array is particularly designed through a series of numerical simulations. It is composed of 32 linear array elements with a central frequency of 1 MHz. The aperture of the probe is 18.6 mm and the equal spacing between the elements is 0.6 mm. The high center frequency of 1 MHz provides sufficient resolution for the debonding defect detection of CFSTs. The time window and the sampling point are set to 80  $\mu$ s and 4000, respectively. A software program is further developed for data pre-processing and image reconstruction in real time, as shown in Fig. 5. It is worth noting that ultrasound coupling gel should be smeared evenly between the probe and the surface of the CFSTs during data acquisition.

## 3. Methodology

### 3.1. Image reconstruction by TFM

A schematic illustration of the TFM imaging algorithm is shown in Fig. 6. Based on the FMC dataset, the TFM algorithm reconstructs an ultrasonic image by superimposing the amplitude of all the echoes at the corresponding travel-time. The two-way travel time  $t_{ij}(x, z)$  of the reflected signal from the  $i$ -th transmitter to an arbitrary imaging point  $(x, z)$  in the subsurface and back to the  $j$ -th receiver is given by

$$t_{ij}(x, z) = \frac{\sqrt{(x - x_i)^2 + z^2} + \sqrt{(x - x_j)^2 + z^2}}{v} \quad (1)$$

where  $x_i$  and  $x_j$  are the  $x$ -coordinates of the receiver and transmitter on the ground surface, and  $v$  represents the propagation velocity of ultrasonic signal in the medium ( $v = 5920\text{m/s}$  in steel). The superposed amplitude at an imaging point  $(x, z)$  can be calculated by stacking the amplitude of the  $N \times N$  reflection signals. Thus, the reconstructed image is obtained by using the following formula [33]

$$E(x, z) = \left| \sum_{i=1}^N \sum_{j=1}^N S_{ij}(t_{ij}(x, z)) \right| \quad (2)$$

where  $S_{ij}(t_{ij}(x, z))$  represents the amplitude of the reflection signal  $S_{ij}$  at the two-way travel-time of  $t_{ij}(x, z)$  recorded by the  $j$ -th receiver and radiated by the  $i$ -th transmitter.

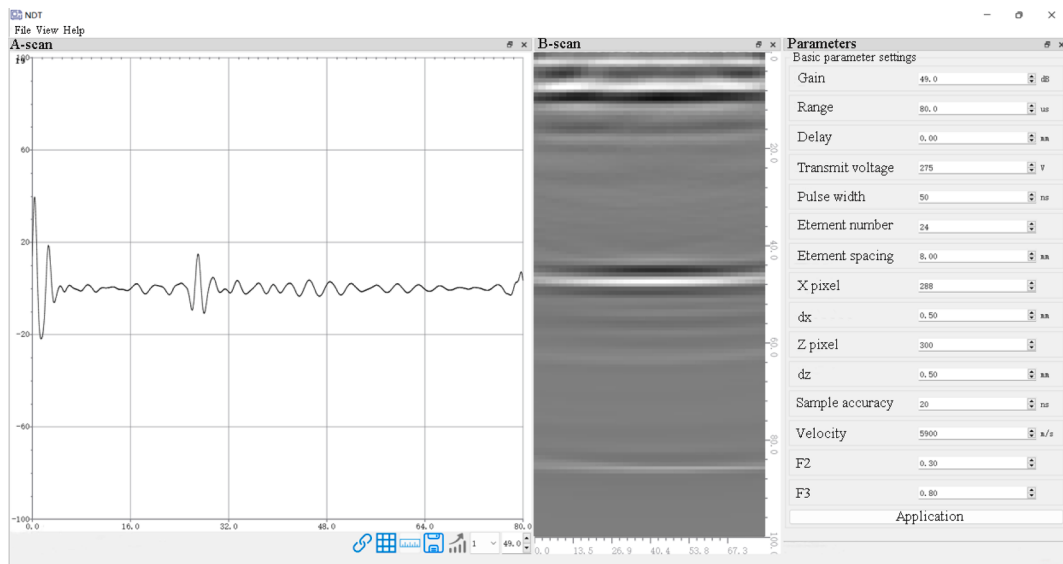
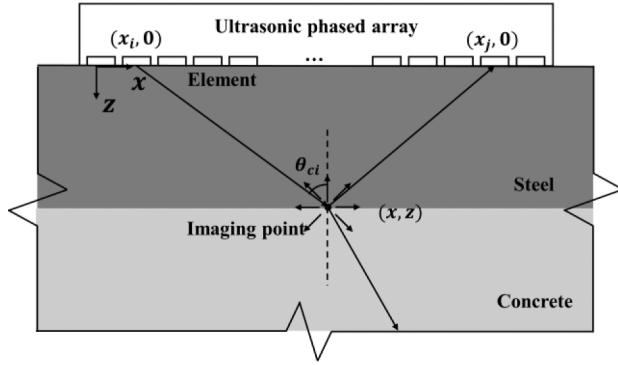


Fig. 5. The developed data processing and imaging software for the ultrasonic phased array system.



**Fig. 6.** Schematic illustration of the TFM imaging algorithm, redrawn from [36].

### 3.2. Debonding evaluation criterion

A debonding evaluation criterion is proposed to determine the location and range of the interfacial debonding defects by calculating the apparent reflection coefficient at the steel-concrete interface. The CFST structural damage level is further semi-quantitatively evaluated according to the debonding rate.

Since the ultrasonic waves excited by the designed ultrasonic phased array are longitudinal waves, a model illustrating the reflection and transmission of longitudinal acoustic waves at an oblique incidence on a solid-solid interface is shown in Fig. 7. The relationship of the incident and reflection angles can be calculated using Snell's Law [31]:

$$\frac{\sin\theta_i}{v_{d1}} = \frac{\sin\theta_{d1}}{v_{d1}} = \frac{\sin\theta_{s1}}{v_{s1}} = \frac{\sin\theta_{d2}}{v_{d2}} = \frac{\sin\theta_{s2}}{v_{s2}} \quad (3)$$

where  $v_s$  and  $v_d$  represent the propagation velocities of the shear wave and the longitudinal wave, respectively,  $\theta_i$  is the incident angle while  $\theta_d$  and  $\theta_s$  are the reflection angles of the longitudinal and shear waves, respectively. The reflection coefficient of the longitudinal waves can be determined by applying Cramer's rule [34]:

$$R_{dd} = \left( \frac{\det[b]}{\det[a]} \right)^2 \frac{\cos\theta_{d1}}{\cos\theta_i} \quad (4)$$

where the vector matrixes **a** and **b** can be calculated from geometrical considerations:

$$a = \begin{bmatrix} -\cos\theta_{d1} & -\cos\theta_{d2} & -\sin\theta_{s1} & \sin\theta_{s2} \\ -\sin\theta_{d1} & \sin\theta_{d2} & \cos\theta_{s1} & \cos\theta_{s2} \\ -Z_{d1}\cos2\theta_{s1} & Z_{d2}\cos2\theta_{s2} & -Z_{s1}\sin2\theta_{s1} & -Z_{s2}\sin2\theta_{s2} \\ -Z_{s1}\frac{v_{s1}}{v_{d1}}\cos2\theta_{s1} & -Z_{s2}\frac{v_{s2}}{v_{d2}}\sin2\theta_{s2} & Z_{s1}\cos2\theta_{s1} & -Z_{s2}\cos2\theta_{s2} \end{bmatrix}$$

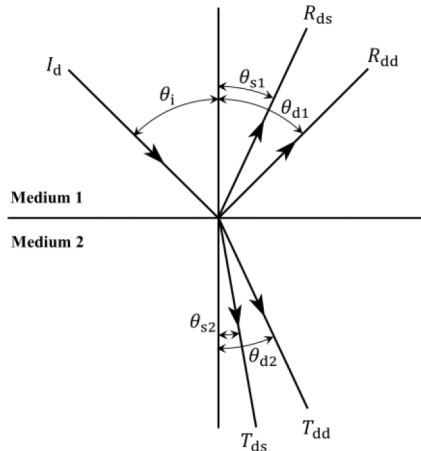


**Fig. 7.** Reflection and transmission of ultrasonic waves for a longitudinal incidence at a solid-solid interface.

$$b = \begin{bmatrix} -\cos\theta_{di} & -\cos\theta_{d2} & -\sin\theta_{s1} & \sin\theta_{s2} \\ \sin\theta_{di} & \sin\theta_{d2} & \cos\theta_{s1} & \cos\theta_{s2} \\ Z_{d1}\cos2\theta_{si} & Z_{d2}\cos2\theta_{s2} & -Z_{s1}\sin2\theta_{s1} & -Z_{s2}\sin2\theta_{s2} \\ -Z_{s1}\frac{v_{s1}}{v_{d1}}\cos2\theta_{di} & -Z_{s2}\frac{v_{s2}}{v_{d2}}\sin2\theta_{s2} & Z_{s1}\cos2\theta_{s1} & -Z_{s2}\cos2\theta_{s2} \end{bmatrix} \quad (5)$$

where  $Z_s$  and  $Z_d$  represent the acoustic impedances of the shear wave and the longitudinal wave, respectively. The impedance can be calculated with  $Z = \rho v$ , and  $\rho$  is the density of the medium.

The acoustic parameters of air, steel and concrete are given in Table 1, and the calculated reflection coefficient curves at a steel-concrete interface and a steel-air interface are shown in Fig. 8(a). The reflection coefficient decreases as the incidence angle increases from zero to approximately  $70^\circ$ , which is equal to the critical angle. When the incident angle is greater than the critical angle, the reflection coefficient increases rapidly towards one. It is worth noting that the energy of the acoustic waves is completely reflected at a normal incidence on the steel-air interface. In the case of the CFST columns of the Shenzhen SEG building (the thickness of the steel tube is about 2 cm and the aperture of the ultrasonic phased array is 18.6 mm), the incidence angle is smaller than  $26^\circ$ . The reflection coefficients on the back interface of the steel tube without a debonding defect are less than 0.41 and those with a debonding defect are greater than 0.61. In reality, the direct measurement of the reflection coefficient is difficult, since the transmitted energy is unknown. Instead, it is proposed to measure the apparent reflection coefficient, which is estimated from the ratio between the reflection amplitude on a steel-concrete interface and that on a steel-air interface. As shown in Fig. 8(b), the apparent reflection coefficient stays almost a constant when the incidence angle is smaller than  $26^\circ$ . A threshold of 0.5 is set to judge whether the tested area of the CFST is debonding or not. In real-world applications, the reflection amplitude of signal from a steel-air interface can be measured with a calibration experiment, and the apparent reflection coefficient can be obtained by

$$RA = \frac{A}{A_{ref}} \quad (6)$$

where  $A$  represents the amplitude of the interface reflection signal of a CFST to be measured and  $A_{ref}$  represents the amplitude of reflection from the free backside of a steel plate with the same thickness as the tube of the CFST.

Because debonding defects are randomly distributed in CFST columns, a partial debonding defect may exist within the imaging region, as illustrated in Fig. 3(a). Thus, the interfacial debonding is judged trace-by-trace and the damage level of a CFST is evaluated with the debonding rate. If the reconstructed image is composed of  $n$  traces within the range of the imaging aperture, the debonding rate is defined by:

$$\chi = \frac{n_{debond}}{n} \quad (7)$$

where  $\chi$  represents the debonding rate,  $n_{debond}$  represents the number of horizontal debonding pixels in the imaging region and  $n$  represents the number of total horizontal pixels. The evaluation criteria are shown in Table 2; i.e., when  $\chi = 0$ , it means that the CFST is well bonded,  $0 < \chi \leq 0.5$  indicates slight debonding,  $0.5 < \chi < 1$  indicates moderate debonding and when  $\chi = 1$ , the CFST is seriously or completely debonded.

Fig. 9 illustrates the data processing flowchart for the evaluation of the debonding defects of CFSTs. The recorded FMC dataset is first processed by a band-pass filter to enhance the signal-to-noise ratio. Then the TFM algorithm is utilized to reconstruct a high-resolution image of the steel interface. Each trace (column) of the reconstructed image is multiplied by a gain curve, and the interface reflection amplitude is extracted and divided by the reflection amplitude recorded in the calibration experiment to calculate the reflection coefficient. Finally, the proposed debonding evaluation criterion is applied to evaluate the debonding ratio.

#### 4. Experiments and results

In this section, we first present a calibration experiment for defining the interface reflection coefficient with a series of steel plates. A verification experiment with 15 boreholes was carried out to verify the detection accuracy of the proposed method. Finally, ultrasonic data were recorded along 34 circumferential survey lines on nine CFST columns in the Shenzhen SEG Building and the debonding damage is evaluated by calculating the comprehensive debonding rates of the columns.

**Table 1**  
Acoustic parameters of the media of a CFST [37].

|   | Air                   | Steel              | Concrete           |
|---|-----------------------|--------------------|--------------------|
| $v_d$ (m/s)                                 | $3.43 \times 10^2$    | $5.90 \times 10^3$ | $4.20 \times 10^3$ |
| $v_s$ (m/s)                                 | $1.00 \times 10^{-5}$ | $3.20 \times 10^3$ | $2.00 \times 10^3$ |
| $\rho$ (kg/m <sup>3</sup> )                 | 1.00                  | $7.90 \times 10^3$ | $2.40 \times 10^3$ |
| $Z_d$ (kg/(s <sup>2</sup> m <sup>2</sup> )) | $3.43 \times 10^2$    | $4.66 \times 10^7$ | $1.01 \times 10^7$ |
| $Z_s$ (kg/(s <sup>2</sup> m <sup>2</sup> )) | $1.00 \times 10^{-5}$ | $2.53 \times 10^7$ | $4.80 \times 10^6$ |

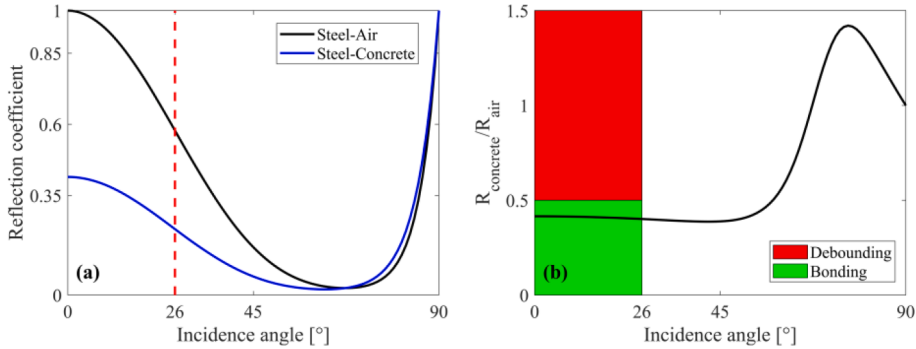


**Fig. 8.** (a) Reflection coefficient curves of longitudinal acoustic waves at steel-air and steel-concrete interfaces and (b) their ratios, i.e., the apparent reflection coefficient used for the debonding evaluation.

**Table 2**  
The evaluation criteria of CFST interfacial debonding.

| Debonding degree   | Debonding ratio |
|--------------------|-----------------|
| Serious debonding  | 100%            |
| Moderate debonding | 50–100%         |
| Slight debonding   | 0–50%           |
| Bonding            | 0%              |

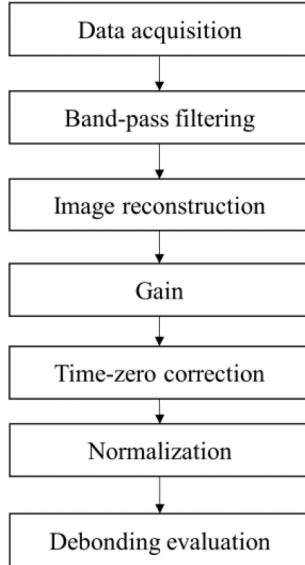


**Fig. 9.** Flowchart of the data processing and debonding evaluation criteria.



**Fig. 10.** Setup of the calibration experiment with steel plates of different thicknesses.

#### 4.1. Calibration experiment for defining reflection coefficient

When ultrasonic waves propagate in a dissipative medium, the ultrasonic energy attenuates gradually with the traveling distance, as a result of geometric spreading, intrinsic attenuation and scattering. Thus, a calibration experiment was carried out to measure  $A_{ref}$  in Eq. (6) for steel tubes with different thicknesses using the designed phased array system, as shown in Fig. 10. In the case of bonding well, a sufficient downforce was applied to the steel plate to ensure that the concrete block is in close contact with a 2.0-cm steel plate. Additionally, four steel plates of different thicknesses including 2.0 cm, 3.0 cm, 4.0 cm and 5.0 cm were placed in the air to simulate the serious debonding scenarios of CFST structures. The ultrasonic phased array probe was set in the center and parallel to the short edge of the steel plate to mitigate the edge interference. To ensure the effective coupling between the probe and the steel plate, petrolatum was smeared evenly on the probe and the measuring area before data acquisition.

In the images reconstructed from the calibration experiment data using a constant ultrasonic velocity ( $v = 5920 \text{ m/s}$ ) in Fig. 11, the back sides of the steel plates are clearly resolved. The reflection signal at the top of the reconstructed images includes direct coupling and surface reflection. Time-zero is set at the position of the surface reflection. The reflection amplitude of the signal from the back of the steel plate in each trace (red point) is extracted for the debonding evaluation of the measurement data in the field. As the thickness of the steel plate increases, the reflection amplitude decreases. A standard gain curve is obtained according to the inverse of the extracted reflection amplitude after smoothing, as shown in Fig. 12. This gain curve is applied to normalize each trace in the reconstructed image from the FMC data acquired in the field.

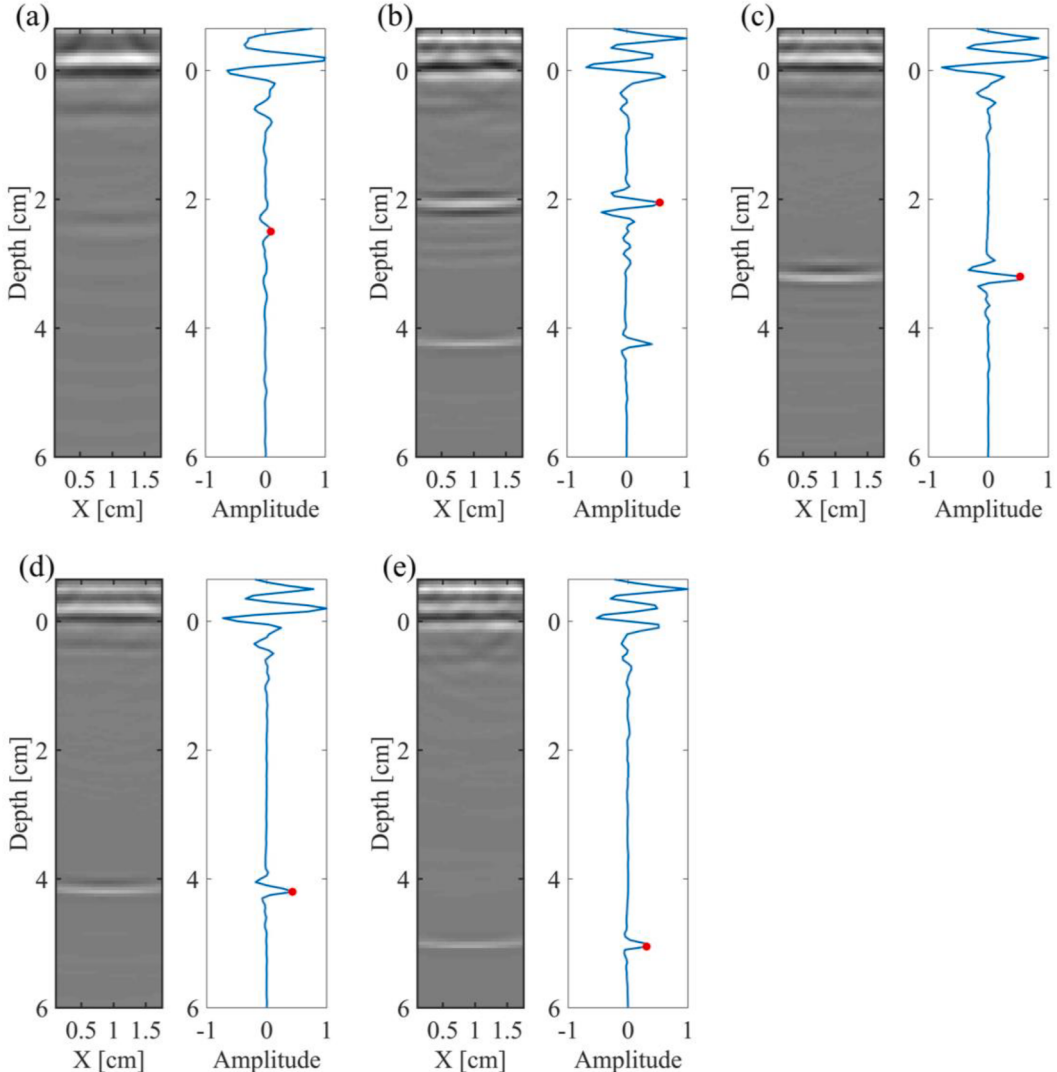


**Fig. 11.** Reconstructed images (left panel) and their mean traces (right panel) for (a) a bonding case and debonding cases with steel plate thicknesses of (b) 2.0 cm, (c) 3.0 cm, (d) 4.0 cm and (e) 5.0 cm.

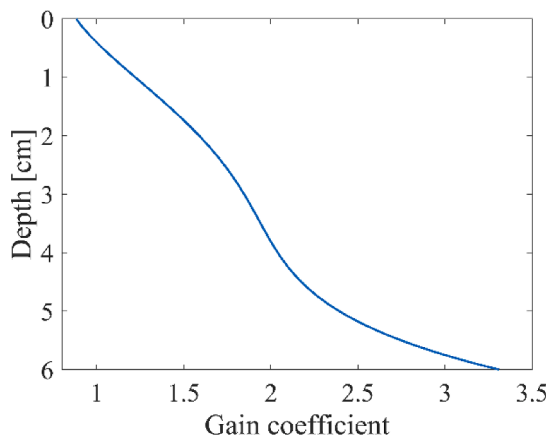


**Fig. 12.** Gain curve obtained from the reflection amplitude recorded in the calibration experiment.

#### 4.2. Borehole verification experiment

Since the SEG building was built in 2000, the external anti-corrosive coating of the CFST columns suffers from damage such as peeling and delamination, which results in a severe interference with the debonding defect identification in the reconstructed acoustic image. Therefore, it is necessary to remove the paint coating and rust within the test area under the phased array probe on the surface of the CFST column. Before the data acquisition, an appropriate coupling agent was smeared on the measuring area and the phased array probe surface to ensure that ultrasonic waves can effectively radiate into the CFST columns.

A field verification experiment was carried out to further validate the effectiveness of the proposed interfacial debonding detection and evaluation method. Fifteen measuring points were selected for data acquisition. An ultrasonic FMC dataset is collected above, below, to the left, and to the right of each borehole, and acoustic images are reconstructed. Then boreholes with a diameter of 3 cm were drilled for verification. The debonding thickness of each borehole was determined by inserting steel patches of different thicknesses into the interstice between the concrete and the steel tube of the CFST columns. The patch testing was conducted above, below, to the left and to the right of each borehole. The results are shown in Table 3. It is worth noting that the term “fail” in Table 3 means that it is difficult to insert a patch with a thickness of 0.05 mm. However, it cannot be confirmed that the measuring area is well bonded because the debonding state may be concealed during the impact drilling.

The results of the apparent reflection coefficient from the mean trace of the reconstructed acoustic image are shown in Fig. 13(a). The apparent reflection coefficients are less than 0.5 at the measuring points where the 0.05-cm steel patch cannot be inserted. When the debonding thickness is equal to or larger than 0.05 mm, the air defect between the steel and the concrete reflects most of the ultrasonic energy and the mean reflection coefficients are larger than 0.5. The statistics of the debonding evaluation results at all 60 measuring points are shown in Fig. 13(b). The debonding status at the measurement points where the steel patch can be inserted is classified as a serious or moderate debonding degree. Some measurement points with a debonding thickness of less than 0.05 mm are judged to be serious debonding, because small debonding defects probably exist in the imaging region, as illustrated in Fig. 3(a). The results of the borehole experiment fully verify the accuracy of the proposed debonding evaluation criterion.

**Table 3**

Patch insertion results of the 15 boreholes for different CFST columns in the Shenzhen SEG Building.

| No. | Tube thickness (mm) | Patch thickness could be inserted |       |      |       |
|-----|---------------------|-----------------------------------|-------|------|-------|
|     |                     | Above                             | Below | Left | Right |
| 1   | 22.4                | fail                              | fail  | 0.20 | fail  |
| 2   | 22.0                | fail                              | fail  | fail | fail  |
| 3   | 21.7                | fail                              | fail  | fail | fail  |
| 4   | 17.3                | fail                              | fail  | fail | fail  |
| 5   | 18.8                | fail                              | fail  | fail | fail  |
| 6   | 19.6                | fail                              | fail  | fail | fail  |
| 7   | 22.4                | fail                              | fail  | fail | fail  |
| 8   | 23.2                | fail                              | 0.10  | fail | fail  |
| 9   | 20.0                | fail                              | fail  | fail | fail  |
| 10  | 20.2                | fail                              | fail  | fail | fail  |
| 11  | 20.0                | 0.10                              | 0.05  | fail | fail  |
| 12  | 25.5                | fail                              | fail  | fail | fail  |
| 13  | 25.4                | 0.20                              | 0.20  | 0.20 | 0.20  |
| 14  | 25.6                | fail                              | fail  | 0.10 | fail  |
| 15  | 25.1                | 0.20                              | 0.20  | fail | 0.20  |

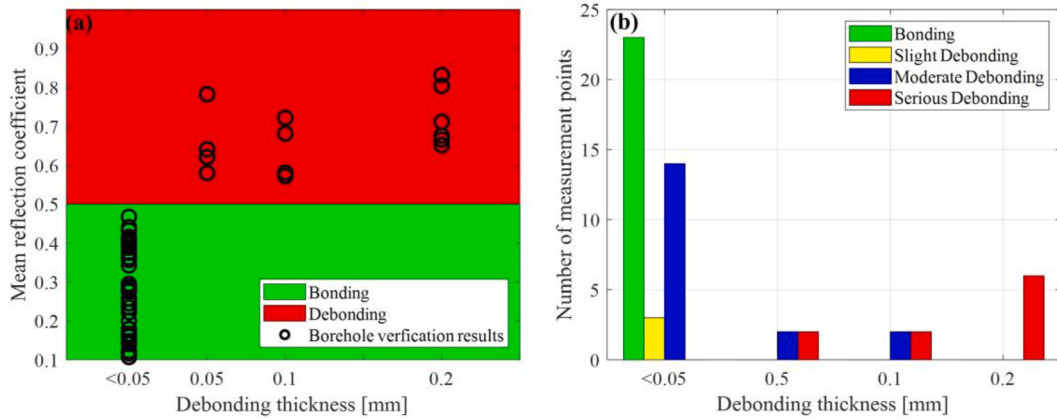


**Fig. 13.** Verification results of 15 boreholes. (a) Mean reflection coefficients and (b) debonding evaluation results.

#### 4.3. Debonding evaluation of CFST columns in the SEG building

To evaluate the debonding status of the frame columns in the Shenzhen SEG Building, nine CFST columns on eight different floors were selected to conduct the acoustic measurement using the developed ultrasonic phased array. Three or four circumferential survey lines were measured on each column, and these survey lines are located at the top, middle and bottom of the column. The paint coating on the surface of the CFST column was removed and the steel tube was polished before data acquisition. The ultrasonic phased array probe was attached to the steel tube wall after smearing the coupling agent, and a measurement station was set every 10 cm along the circumferential survey line to collect FMC datasets. Then, the aforementioned data processing flow is used to detect the debonding defects and to evaluate the debonding rate of the CFST columns. The procedures of the data collection and processing are illustrated in Fig. 14. At the last step, a comprehensive debonding rate of each measurement ring is calculated by

$$\omega = \frac{0.25n_2 + 0.75n_3 + 1.0n_4}{n_1 + n_2 + n_3 + n_4} \quad (8)$$

where  $n_1$ ,  $n_2$ ,  $n_3$  and  $n_4$  denote the number of measuring stations where the steel tube is bonding well, and has slight debonding, moderate debonding and serious debonding on the circumferential survey line, respectively.

Fig. 14(b) delineates the location and extension of the debonding defects along the circumferential ring. It is worth noting that partial debonding defects may exist even in a small area under the phase array probe, as shown in Fig. 14(c). Overall, the moderate or serious debonding defects are continuous. Fig. 15 illustrates the interfacial debonding evaluation results from three typical floors. The results show that the damage degrees of the haunch and shoulder survey lines are much more severe than that of the bottom survey line. The debonding region can reach one-third of the cross section. In addition, some isolated interfacial debonding defects with small proportions can also be detected. In the debonding evaluation result of the basement floor shown in Fig. 15(c), there is no measuring point judged to have "serious debonding". Table 4 presents the estimated debonding rates of the 34 survey lines on the nine CFST columns in the Shenzhen SEG Building. The results show that the interfacial debonding rates at different positions are widespread. The comprehensive debonding rates of nearly half of the survey lines are greater than 50%. The maximum debonding rate is 86.0% and the average debonding rate is 46.6%. Furthermore, the debonding rates in the middle of the columns are higher and the debonding damage is more serious than those at the top and bottom of the columns. The upper part of the whole building suffers from a high debonding rate while the basement has a light damage degree. The reason for this may be that the upper floors are strongly affected by the wind load, and the inter-story displacement is larger than that of the lower floors, resulting in the serious debonding of the CFST columns on the upper floors.

#### 5. Discussion

In this paper, we propose a semi-quantitative detection method using an ultrasonic phased array for interfacial debonding evaluation in CFST columns. However, this method can only localize the debonding region, it cannot determine the debonding thickness. A thin debonding layer model is introduced to explain the reflection and transmission of ultrasonic waves, as shown in Fig. 16(a). When the ultrasonic waves pass through a thin air layer between steel and air, it causes multiple reflections and transmissions at the interfaces on both sides of the thin layer. The reflectivity related to the thin air gap between steel and concrete can be expressed by [35]

$$R = 1 - \frac{4Z_1 Z_3}{(Z_1 + Z_3)^2 \cos^2 \frac{2\pi d_2}{\lambda_2} + (Z_2 + \frac{Z_1 Z_3}{Z_2})^2 \sin^2 \frac{2\pi d_2}{\lambda_2}} \quad (9)$$

where  $Z_1$ ,  $Z_2$ , and  $Z_3$  represent the ultrasound impedances of steel, air and concrete, respectively, which are calculated with  $Z = \rho v$ .  $\rho$  and  $v$  represent the ultrasound velocity and density of the medium,  $\lambda$  is the ultrasonic wavelength and  $d$  is the thickness of the thin air

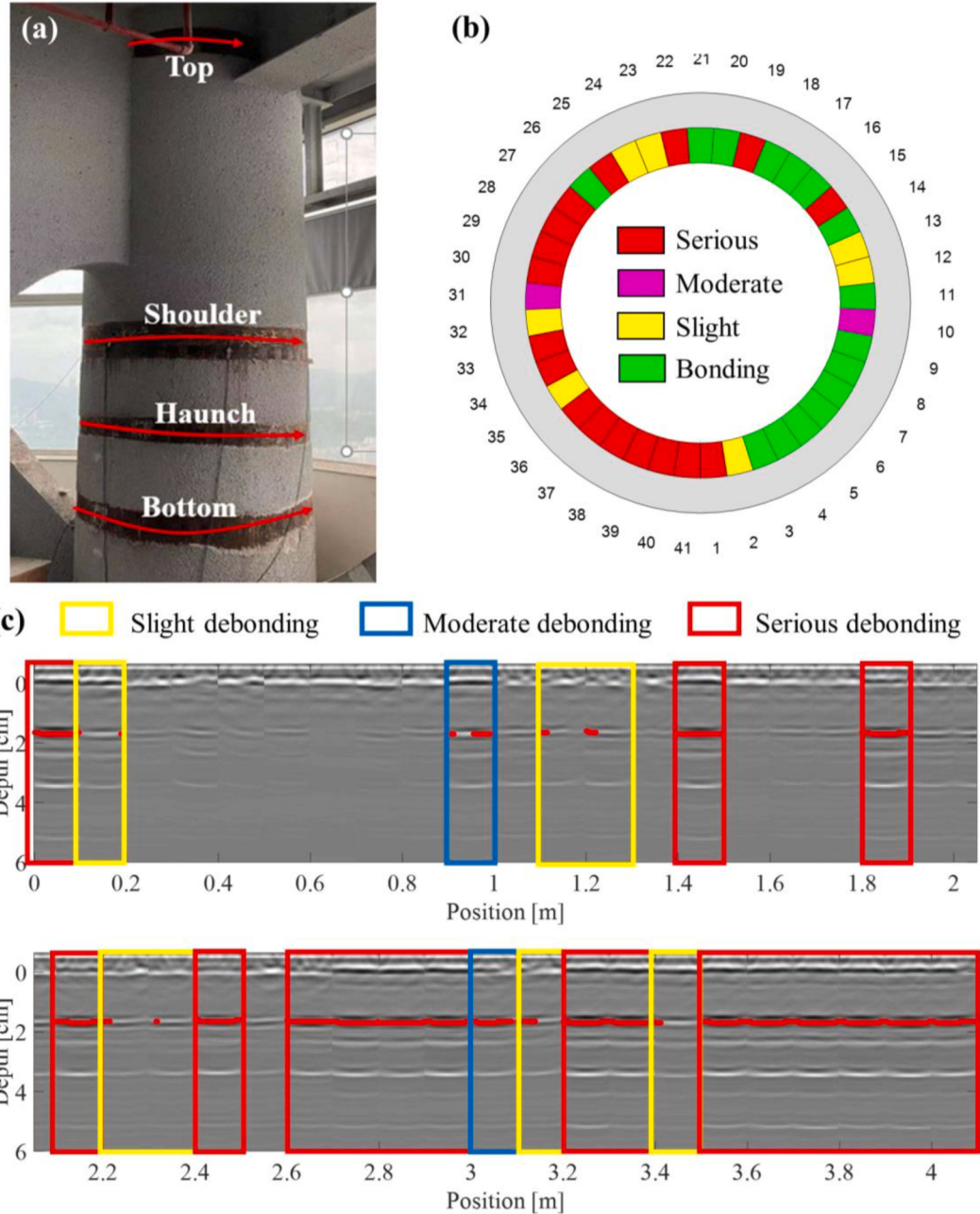


**Fig. 14.** Field experiment setup and the data processing flow. (a) Arrangement of survey lines, (b) the interfacial debonding evaluation result and (c) a series of reconstructed acoustic images along a circumferential survey line. The red points marked on the interface reflection indicate the debonding points, where the apparent reflection coefficient is larger than 0.5. (For interpretation of the references to colour in this figure legend, the reader is referred to the web version of this article.)

gap between the steel and the concrete. These material parameters are given in Table 4. Fig. 15(b) illustrates the reflectivity curve of the steel-air-concrete model. The central frequency of the excitation signal is 1 MHz, which is consistent with the developed phased array probe. Consequently, total reflection occurs when the debonding thickness is greater than  $10^{-7}$  mm due to the huge impedance difference between steel and air. In other words, as long as the CFST has an interfacial debonding defect, no matter how thick the defect is, the incident ultrasonic waves are totally reflected. Due to the limitation of the resolution of the developed ultrasonic phased array, it is difficult to estimate the interfacial debonding thickness in the reconstructed ultrasonic image.

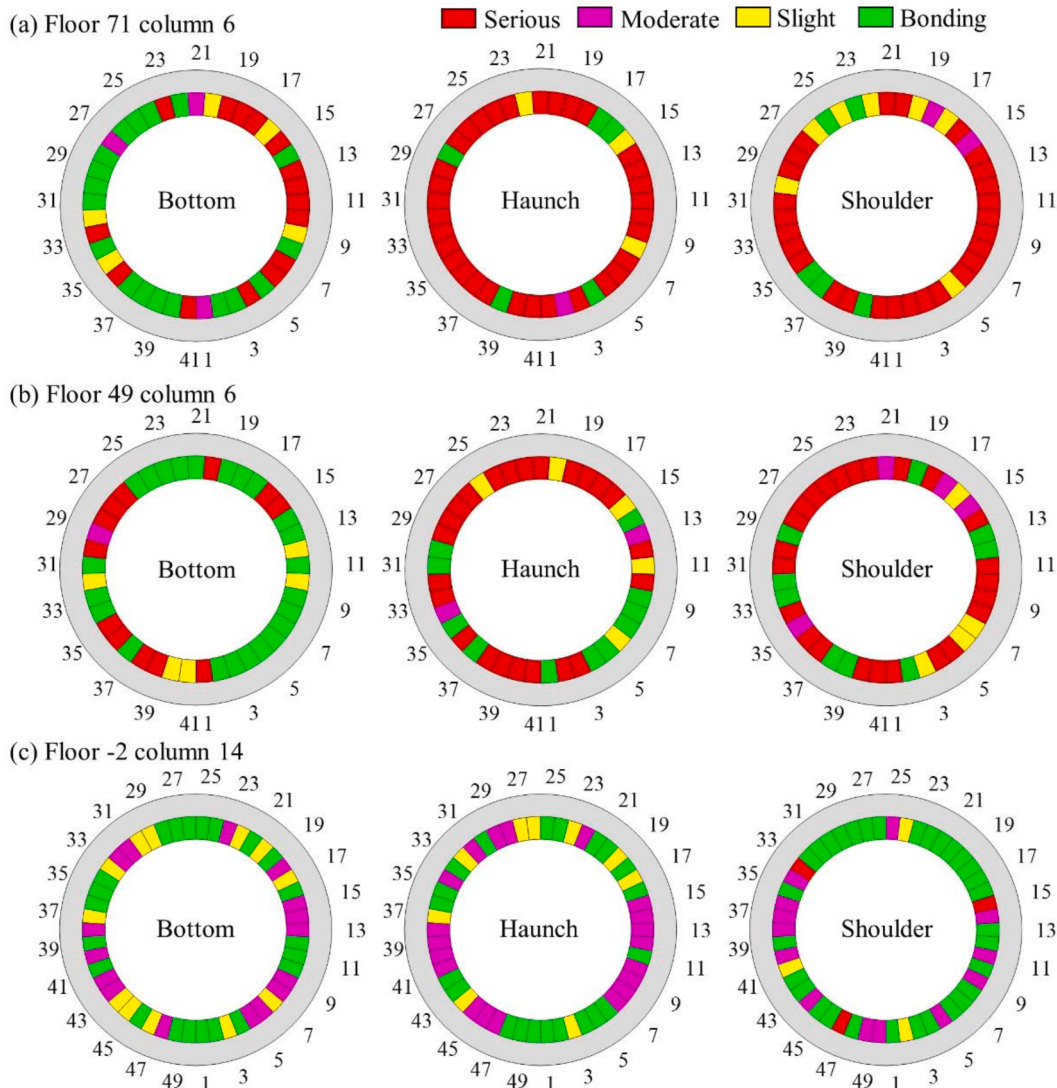


**Fig. 15.** The interfacial debonding evaluation results of the bottom (left panel), haunch (middle panel), and shoulder (right panel) survey lines of the CFST columns in the (a) 71st floor, (b) 49th floor and (c) -2nd floor.

**Table 4**

Comprehensive debonding rates of nine CFST columns in the SEG Building. The number in bold indicates the circumferential survey ring on a single CFST column with the highest debonding rate.

| Floor          | Column | Survey lines |              |              |              | Average      |
|----------------|--------|--------------|--------------|--------------|--------------|--------------|
|                |        | Bottom       | Haunch       | Shoulder     | Top          |              |
| 71             | 6      | 45.1%        | <b>81.7%</b> | 73.8%        | 32.5%        | 58.3%        |
| 71             | 16     | 16.3%        | <b>86.0%</b> | 54.9%        | 25.0%        | 45.6%        |
| 70             | 4      | 8.1%         | 49.4%        | <b>77.3%</b> | 33.3%        | 42.0%        |
| 63             | 1      | 60.0%        | 68.9%        | 34.2%        | <b>85.7%</b> | 62.2%        |
| 49             | 6      | 34.2%        | 62.8%        | <b>68.3%</b> | 62.5%        | 57.0%        |
| 34             | 2      | 37.5%        | <b>61.4%</b> | 28.4%        | 8.3%         | 33.9%        |
| 19             | 2      | 66.0%        | <b>73.4%</b> | 57.5%        | 35.0%        | 58.0%        |
| -2             | 14     | 24.5%        | 34.5%        | 27.0%        | —            | 28.7%        |
| -4             | 14     | 29.7%        | 32.5%        | 38.5%        | —            | 33.6%        |
| <b>Average</b> |        | 35.7%        | <b>61.2%</b> | 51.1%        | 40.3%        | <b>46.6%</b> |

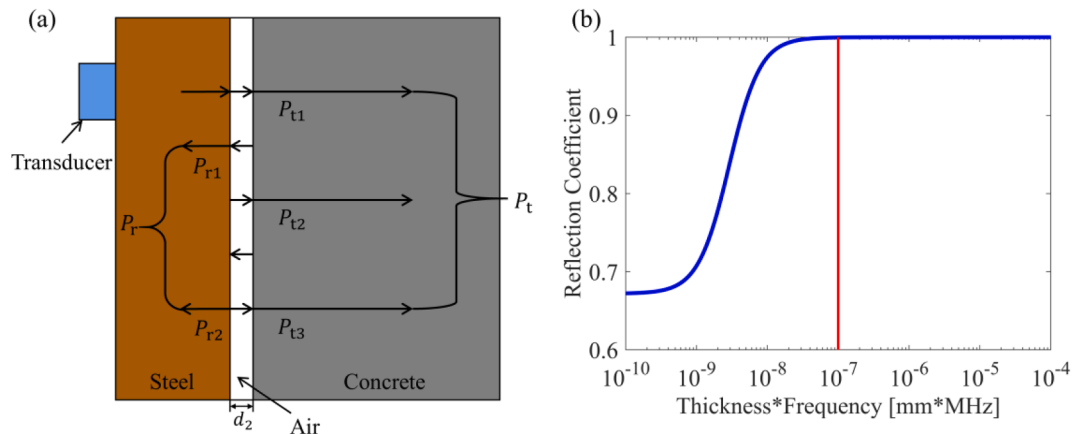


**Fig. 16.** (a) A steel-air-concrete thin layer model and (b) the reflection coefficient curve.

## 6. Conclusions

In this paper, an imaging-based method using an ultrasonic phased array is proposed for the interfacial debonding detection and evaluation of CFSTs. To balance imaging resolution and inspection efficiency, the TFM algorithm is adopted for image reconstruction. The apparent reflection coefficient of the signal from the backside of the steel tube in the reconstructed image is introduced for debonding detection and localization. According to the reflection coefficient curve, a threshold of 0.5 is set to judge whether the tested area of the CFST is debonding or not. The debonding degree at each measurement point is divided into four grades according to the debonding rate. The proposed inspection method can be used to locate the debonding region and determine the debonding size to achieve a semi-quantitative evaluation of the debonding defects. The steel patch insertion results of the 15 boreholes in the Shenzhen SEG building show that the interfacial debonding defects can be accurately detected. The debonding evaluation results recorded from 34 circumferential survey lines of the nine CFST columns in the Shenzhen SEG Building show the severe damage status of the CFSTs with an average debonding rate of 46.6%. Therefore, it is imperative to conduct routine inspections and evaluations for existing CFST structures.

The quantitative detection of debonding thickness in CFSTs is still technically challenging. In future work, numerical simulation and laboratory experiments will be carried out to investigate the influence of CFST debonding on the damping ratio and other dynamic properties of a high-rise CFST structure. In addition, data acquisition was currently carried out point-by-point, which results in a poor detection efficiency for the inspection of a whole building or bridge. In future work, a distance-measuring encoder will be equipped for the ultrasonic phased array system to achieve continuous data acquisition to improve the detection efficiency.

## Declaration of Competing Interest

The authors declare that they have no known competing financial interests or personal relationships that could have appeared to influence the work reported in this paper.

## Data availability

Data will be made available on request.

## Acknowledgements

This paper was supported by the National Natural Science Foundation of China (51978182, 5202010500, 52179126), the Basic and Applied Basic Research Foundation of Guangdong Province, China (2021A1515010881, 2021B1515130006), and the Science and Technology Projects in Guangzhou, China (20210201444, 202206010017).

## References

- [1] F. Alatshani, S.A. Osman, R. Hamid, F. Mashiri, Stiffened concrete-filled steel tubes: A systematic review, *Thin-Walled Struct.* 148 (2020), 106590.
- [2] J. Liu, Y.J. Liu, C.Y. Zhang, Q.H. Zhao, Y. Lyu, L. Jiang, Temperature action and effect of concrete-filled steel tubular bridges: A review, *J. Traffic Transp. Eng.* 7 (2020) 174–191.
- [3] J.L. Zheng, J.J. Wang, Concrete-filled steel tube arch bridges in China, *Engineering* 4 (2018) 143–155.
- [4] L.H. Han, W. Li, R. Bjørhovde, Developments and advanced applications of concrete-filled steel tubular (CFST) structures: Members, *J. Constr. Steel Res.* 100 (2014) 211–228.
- [5] W. Dong, Z.M. Wu, X.M. Zhou, Y.J. Tan, Experimental studies on void detection in concrete-filled steel tubes using ultrasound, *Constr. Build. Mater.* 128 (2016) 154–162.

- [6] Y.T. Guo, X. Nie, M.X. Tao, S.Y. Qiu, L. Tang, J.S. Fan, Bending capacity of steel-concrete-steel composite structures considering local buckling and casting imperfection, *J. Struct. Eng.* 145 (2019) 04019102.
- [7] L.L. Duan, X. Nie, R. Ding, L.D. Zhuang, Research on application of uplift-restricted slip-permitted (URSP) connectors in steel-concrete composite frames, *Appl. Sci.-Basel* 9 (2019) 2235–2256.
- [8] J.Q. Xue, B. Briseghella, B.C. Chen, Effects of debonding on circular CFST stub columns, *J. Constr. Steel Res.* 69 (2012) 64–76.
- [9] Shenzhen SEG Building experienced shaking, experts to the scene for safety testing, The Xinhua News Agency, 2021.
- [10] Z. Zu, Expert: The reason for the vibration of Shenzhen SEG Plaza Building is the wind-induced vortex induced resonance of the mast and the mast needs to be removed, China News Service (2021).
- [11] Inspection report of Shenzhen SEG Building, Guangzhou University, 2021.
- [12] F.Y. Liao, L.H. Han, Z. Tao, Behaviour of CFST stub columns with initial concrete imperfection: Analysis and calculations, *Thin-Walled Struct.* 70 (2013) 57–69.
- [13] H.B. Chen, X. Nie, S.Y. Gan, Y.D. Zhao, H.H. Qiu, Interfacial imperfection detection for steel-concrete composite structures using NDT techniques: A state-of-the-art review, *Eng. Struct.* 245 (2021).
- [14] H. Liu, J.Y. Zhong, F. Ding, X. Meng, C. Liu, J. Cui, Detection of early-stage rebar corrosion using a polarimetric ground penetrating radar system, *Constr. Build. Mater.* 317 (2022), 125768.
- [15] Y. Jun, Clustering of spatially relevant audio data using mel-frequencycepstrum for diagnosis of concrete structure by hammering test, Proceedings of the 2017 IEEE/SICE International Symposium on System Integration, 2017.
- [16] D.D. Chen, V. Montano, L.S. Huo, S.L. Fan, G.B. Song, Detection of subsurface voids in concrete-filled steel tubular (CFST) structure using percussion approach, *Constr. Build. Mater.* 262 (2020), 119761.
- [17] B. Xu, T. Zhang, G.B. Song, H.C. Gu, Active interface debonding detection of a concrete-filled steel tube with piezoelectric technologies using wavelet packet analysis, *Mech. Syst. Sig. Process.* 36 (2013) 7–17.
- [18] J. Zhang, Y. Li, G. Du, G. Song, Damage detection of L-shaped concrete filled steel tube (L-CFST) columns under cyclic loading using embedded piezoceramic transducers, *Sensors (Basel)* 18 (2018) 1–22.
- [19] B. Xu, Diaphragm interface debonding detection of a large-scale irregular MC-CFST column with impedance measurements 7th International Conference on Structural Health Monitoring of Intelligent Infrastructure, 2015.
- [20] Y. Shen, S. Hirose, Y. Yamaguchi, Dispersion of ultrasonic surface waves in a steel–epoxy–concrete bonding layered medium based on analytical, experimental, and numerical study, *Case Stud. Nondestr. Test. Eval.* 2 (2014) 49–63.
- [21] T.L. Jiang, Zhoutao, Tian, Zhongchu, Investigation and application on monitoring the compactness of concrete-filled steel tube structures with ultrasonic wave, *Earth and Space* (2014) 682–689.
- [22] X. Li, M. Luo, C. Hei, G. Song, Quantitative evaluation of debond in concrete-filled steel tubular member (CFSTM) using piezoceramic transducers and ultrasonic head wave amplitude, *Smart Mater. Struct.* 28 (2019).
- [23] H. Xu, Z.Q. Su, L. Cheng, J.L. Guyader, P. Hamelin, Reconstructing interfacial force distribution for identification of multi-debonding in steel-reinforced concrete structures using noncontact laser vibrometry, *Struct. Health Monit.* 12 (2013) 507–521.
- [24] J.C. Yan, W.S. Zhou, X. Zhang, Y.Z. Lin, Interface monitoring of steel-concrete-steel sandwich structures using piezoelectric transducers, *Nuclear, Eng. Technol.* 51 (2019) 1132–1141.
- [25] H. Song, J.S. Popovics, Characterization of steel-concrete interface bonding conditions using attenuation characteristics of guided waves, *Cem. Concr. Compos.* 83 (2017) 111–124.
- [26] A. Velichko, P.D. Wilcox, D.O. Thompson, D.E. Chimenti, Post-processing of the full matrix of ultrasonic transmit-receive array data for guided wave pipe inspection, *AIP Conf. Proc.* (2009).
- [27] H. Liu, Z.J. Chen, H.T. Lu, F. Han, C. Liu, J. Li, J. Cui, Migration of ground penetrating radar with antenna radiation pattern correction, *IEEE Geosci. Remote Sens. Lett.* 19 (2022) 1–5.
- [28] J. Zhang, B.W. Drinkwater, P.D. Wilcox, A.J. Hunter, Defect detection using ultrasonic arrays: The multi-mode total focusing method, *NDT E Int.* 43 (2010) 123–133.
- [29] J. Zhang, B.W. Drinkwater, P.D. Wilcox, Effects of array transducer inconsistencies on total focusing method imaging performance, *NDT E Int.* 44 (2011) 361–368.
- [30] H. Liu, H.Y. Xia, M.W. Zhuang, Z.J. Long, C. Liu, J. Cui, B. Xu, Q.F. Hu, Q.H. Liu, Reverse time migration of acoustic waves for imaging based defects detection for concrete and CFST structures, *Mech. Syst. Sig. Process.* 117 (2019) 210–220.
- [31] H. Liu, Z.J. Long, F. Han, G.Y. Fang, Q.H. Liu, Frequency-domain reverse-time migration of ground penetrating radar based on layered medium Green's functions, *IEEE J. Sel. Top. Appl. Earth Obs. Remote Sens.* 11 (2018) 2957–2965.
- [32] D. Douglas R, A 256-Element Ultrasonic Phased Array System for the Treatment of Large Volumes of Deep Seated Tissue, *IEEE Transactions on Ultrasonics, Ferroelectrics, and Frequency Control*, 46 (1999) 1254–1268.
- [33] S. Beniwal, D. Ghosh, A. Ganguli, Ultrasonic imaging of concrete using scattered elastic wave modes, *NDT E Int.* 82 (2016) 26–35.
- [34] R.L. Joesph, *Ultrasonic Waves in Solid Media*, Cambridge University Press, 2003.
- [35] H. Zheng, *Ultrasonic testing*, China Labor and Social Security Publishing House, 2008, pp. 36–38, in Chineses.
- [36] C. Holmes, B.W. Drinkwater, P. Wilcox, The post-processing of ultrasonic array data using the total focusing method, *Insight* 46 (2004) 677–680.
- [37] A.P. Boresi, *Advanced Mechanics Of Materials*, Wiley India, New Delhi, 2009, pp. 10–15.